Commun Nonlinear Sci Numer Simulat 15 (2010) 1538–1552

Contents lists available at ScienceDirect

Commun Nonlinear Sci Numer Simulat

journal homepage: www.elsevier.com/locate/cnsns

Simulations of collision of ice particles

Piroz Zamankhan

Faculty of Industrial Engineering, Mechanical Engineering and Computer Sciences, University of Iceland, Hjardarhagi 2-6, IS-107 Reykjavik, Iceland

ARTICLE INFO

Article history:
Received 6 February 2009
Received in revised form 28 June 2009
Accepted 30 June 2009
Available online 7 July 2009

PACS:
92.40.–t
92.40.vx

Keywords:
Ice–structure interactions
Collisions
Element free Galerkin methods
Fracture

ABSTRACT

The objective of this paper is to develop a realistic model for ice–structure interaction. To this end, the experiments made by Bridges et al. [Bridges FG, Hatzes A, Liu DNC. Structure, stability and evolution of Saturn's rings. Nature 1984;309:333–5] in order to measure the coefficient of restitution for ice particles are thoroughly analyzed. One particularly troublesome aspect of the aforementioned experiments is fracture of the ice particles during a collision. In the present effort, the collisional properties of the ice particles are investigated using a Finite Element approach. It is found that a major challenge in modeling collision of the ice balls is the prediction of the onset of fracture and crack propagation in them. In simulations of a block of ice collision to a structure, it is crucial that fracture is determined correctly, as it will influence the collisional properties of the ice particles. The results of the simulation, considering fracture criterion implemented into the Finite Element Model [Zamankhan P, Bordbar M-H. Complex flow dynamics in dense granular flows. Part I: experimentation. J Appl Mech (T-ASME) 2006;73:648–57; Zamankhan P, Huang J. Complex flow dynamics in dense granular flows. Part II: simulations. J Appl Mech (T-ASME) 2007;74:691–702] together with a material model for the ice, imply that most of the kinetic energy dissipation occurs as a result of fracturing at the contact surface of the ice particles. The results obtained in the present study suggest that constitutive models such as those proposed by Brilliantov et al. [Brilliantov NV, Spahn F, Hertzsch JM, Poschel T. Model for collisions in granular gases. Phys Rev E;1996;53:5382–92] for collisions of ice particles are highly questionable.

1. Introduction

Ice refers to any of the solid form of H_2O [1]. Ice possesses 12 different crystal structures as well as two amorphous states [2]. It plays a key role in activities as diverse as skiing, polar marine transportation, and cold ocean oil exploration. In addition, ice is a factor in global climate, because the Antarctic and Greenland ice sheets cover approximately 10% of the Earth's land area. Ice is also a major constituent of the extraterrestrial bodies [3].

Sea ice is a conglomerate of fresh water crystals interlaced with inclusions of brine, air and salt which have formed between crystals and crystal plates [4]. During World war II, icebergs were proposed as potential aircraft carrier in the Atlantic [5]. Hence, an extensive study of ice as a material had begun in order to provide a better understanding of its mechanical behavior. However, it has become evident that the tensile strength of ice was very much lower than the compressive strength, so that it was not up to the task. It is interesting that the addition of wood pulp can increase the strength, and the shock resistance of ice [2].

Ice is nonhomogeneous and anisotropic. Unlike classical materials, the failure pressures on ice in field tests have been found to be substantially lower than the values that have been recorded at the laboratory scale, which is regarded as scale effect.

E-mail address: piroz@hi.is

1007-5704/$ - see front matter © 2009 Elsevier B.V. All rights reserved.
doi:10.1016/j.cnsns.2009.06.029

Nomenclature

A_{pq}	weighted moment matrix
B_{lq}	matrix
a	height of ice block
b	height of wedge
C	first Cowper–Symonds strain rate parameter
d	ice ball diameter
E	Young's modulus
E_p	plastic hardening modulus defined as $\left(\frac{1}{E_p}=\frac{1}{E}+\frac{1}{E_t}\right)$
E_t	tangential modulus
e_N	coefficient of normal restitution
e_{ij}	deviatoric part of the strain tensor
G_0	instantaneous (glassy) shear modulus
G_∞	long time shear modulus
l_w	length of wedge
m	number of terms of polynomial basis $p(X_j)$
n	number of nodes used in the support domain for constructing the shape function
$p(X_j)$	polynomial basis
q	second Cowper–Symonds strain rate parameter
S_{ij}	deviatoric part of the stress tensor
T	ice temperature (K)
V_{imp}	impact velocity
$u_i(X_j,t)$	displacement field $(u_i=x_i-X_i)$
$u_i^{(h)}$	approximation of u_i
u_l	nodal parameters
$V_i^{(0)}$	initial velocities
V_x	ice ball axial velocity before collision
V_x'	ice ball axial velocity after collision
V_z^*	normalized velocity
V_z	ice block velocity
W	weight function
X_i	Fixed rectangular Cartesian coordinate system $(i=1,2,3)$
$\boldsymbol{X}$	vector notation for X_i
$x_i(X_j,t)$	position of a point at time t in the X_i coordinate system
x, y, z	Cartesian coordinate system
z'	vertical axis as shown in Fig. 7(b)
t	time
t_c	collision time

Greek symbols

β	hardening parameter
δ_{ij}	Kronecker delta
δ_z	vertical distance of cutting xz planes from the base plane as illustrated in Fig. 7(b)
ε_{ij}	strain tensor
ε	axial strain
ε_p	plastic strain (effective)
$\dot{\varepsilon}$	strain rate
Φ_s	distortional relaxation function
Φ_v	volumetric relaxation function
ϕ	MLS shape function
ν	Poisson's ratio
ρ	density
θ	angle of wedge
σ_{ij}	stress tensor
σ_c	peak stress
σ_1	major stress
σ_2	minor stress
σ_Y	yield stress
σ_0	initial yield stress
τ	relaxation time

As mentioned earlier, ice in nature contains flaws, large cracks and leads, entrained air bubbles or dirt, and irregular grain size and composition, each of which has different scale effects. On the scale of individual floes, the ice cover is homogeneous and highly anisotropic. Whereas on the scales as large as several hundred kilometers, the ice cover is nonhomogeneous and behaves practically as isotropic medium. While a great deal of effort has previously been devoted to the study of the scale effect, it is not yet fully understood.

The combination of the scale effect and the inherently heterogeneous structure of ice make it a complex material. Hence, the use of numerical modeling becomes inevitable for the assessment ice loads on structures and vessels during the passage of anomalous atmospheric-pressure fields. In this case, the internal forces in the sea ice field could present one of the most hazardous conditions for constructions of oil exploration industries working in the sea-ice field [6]. In fact, a number of observed phenomena are expected to emerge from numerical simulation if the improved knowledge of the material behavior of ice can be provided.

The elastic behavior of ice is characterized by moderate anisotropy. Drouin and Michel have performed tests on a laboratory sample of columnar ice (type I) whose preferred vertical orientation is the normal to the basal plane, which represents the parallel plane of the molecular structure [7]. The average and maximum Young's modulus measured were found to be 6300 and 8000 MPa, respectively, where the maximum value was obtained with perfect vertical ice grains. Lindgren [8] has proposed an expression for Young's modulus as a function of temperature for columnar ice (type I), given as

$$E_i = 6600(4.276 - 0.012T_i) \tag{1}$$

where E_i is in MPa.

Drouin and Michel [7] have also measured Young's modulus of columnar ice (type II) whose preferred horizontal orientation is the normal to the basal plane. A much lower Young's modulus for columnar ice (type II) has been reported varying from 3000 to 5700 MPa. They have also noticed a greater impact of temperature on Young's modulus for ice (type II) than for ice (type I) [7].

Inelastic behavior is markedly anisotropic, which leads to the build-up of internal stresses that arise because grains favorably oriented for slip shed load to those less well oriented. Therefore, if time is much shorter than the relaxation time of the internal stresses, then plastic flow during impact will initiate cracks. Hatzes et al. [9] have carried out tests on the impact properties of ice. Their results clearly indicated that collisional properties of ice spheres at low and relatively high impact velocities (at 150–175 K) were sensitively determined by their surface structure. In fact, if the surface of ice spheres is very smooth, the collisions would be nearly elastic even at relatively high impact velocities.

In general, the collisions were found to be partially inelastic [9], and the fractional energy loss in impact was given by $(1 - e_N^2)$, where e_N represents the coefficient of normal restitution. Like most solid substances [10], e_N for ice decreases with increasing impact velocity, V_{imp}.

Brilliantov et al. [11] have used the results of Bridges et al. [3] in order to validate their model for the colliding viscoelastic grains. As mentioned earlier, most of the kinetic energy dissipations in tests as detailed in [3,9] occurred as a result of fracturing at the contact surface area of the ice particles. Thus, it is not entirely clear to what extent the collision model of [11] is relevant to the collision of ice particles.

The aforementioned issue have prompted the research reported herein, which investigates collisional properties of the ice particles (especially in relating fracturing on the small scale to that on the larger scale) using computer simulations. Notice that at low rates of deformation (namely, 10^{-7} 1/s), cracks may not form, and ice is ductile. At high rates greater than 10^{-3} 1/s, which occur in collisions, cracks do initiate, and ice is brittle independent of stress state [2].

A number of methods have been developed for the simulation of fracture mechanics problems. Finite element methodology specific to the analysis of the fracture processes has been reviewed by Liebowitz and Moyer Jr. [12]. The boundary element method [13] sharply reduces the efforts for the remeshing since only the line or surfaces representing the cracks in a cracked body need to be remeshed. The element-free Galerkin (EFG) method [14], which utilizes the gridless method for solving the governing partial differential equations, has been proved to offer many attractive features in the modeling of crack propagation. In this technique the domain is filled with nodes and the integration points and the domain boundary is explicitly represented. On the other hand, the displacement interpolant and its gradient are obtained applying a moving least-square interpolation to the nodes that lie within the domain of support of a given integration point. However, in the vicinity of the domain boundary, which could be an extending crack, only nodes that can be reached by a straight line that does not pass through the boundary are included in the domain of influence for a given integration point. Hence, the set of nodes within the domain of influence of an integration point in the vicinity of an extending crack may change abruptly as the crack advances.

This article begins with Section 2, in which a description is presented for transition from continua [15] to discontinua. In Section 3, computer simulations are presented of the collision between an ice ball (that is attached to a pendulum) and a stationary block of ice. A stress–strain curve is used to describe brittle behavior of ice particles that sets in at high strain rates. In Section 4, ice–structure interactions are discussed for which multi-axial stress states are generated within the contact zone. The confinement raises the failure stress with the effect being greater within the regime of brittle behavior that may result in crack growth in ice with arbitrary and complex paths. Finally, conclusions and recommendations are being made in Section 5.

2. Transition from continua to discontinua

The model as detailed in [15,16] is robust and has been thoroughly developed for collision between viscoelastic particles. In brief, the general equations of motion in referential coordinates for 3D isotropic, viscoelastic solids with a volume Ω and a surface boundary Γ, may be given as [15]

$$\rho\ddot{u}_i = \sigma_{ij,j}, \tag{2}$$

where covariant differentiation is represented by the comma-subscript convention, and the superpositioned dot represents the operation of material differentiation.

Eq. (2) with constitutive equation

$$\sigma_{ij} = S_{ij} + \frac{1}{3}\delta_{ij}\sigma_{kk}, \tag{3}$$

and the geometric equations $\varepsilon = 1/2(u_{i,j} + u_{j,i})$, provide 15 equations for 15 unknowns, comprising six stresses σ_{ij}, six strains ε_{ij}, and three displacements u_i. In Eq. (2), $S_{ij} = \int_0^t \Phi_s(t-t')\,de_{ij}/dt'$, $\sigma_{kk} = \int_0^t \Phi_v(t-t')\,d\varepsilon_{kk}/dt'$, and $\varepsilon_{ij} = e_{ij} + \frac{1}{3}\delta_{ij}\varepsilon_{kk}$. Here, Φ_s and Φ_v are distortional and, volumetric relaxation function, respectively [17].

The set of above-mentioned equations has to be solved for initial conditions

$$u_i(X_j, 0) = 0, \tag{4}$$

$$\dot{u}(X_j, 0) = V_i^{(0)}(X_j), \tag{5}$$

and the traction boundary conditions

$$\sigma_{ij}n_j = T_i(t), \tag{6}$$

on boundary Γ_1, and the displacement boundary conditions

$$u_i(X_j, t) = D_i(t), \tag{7}$$

on boundary Γ_2. Notice that the contact discontinuity along an interior boundary Γ_3 (when $u_i^+ = u_i^-$) is given as $\left(\sigma_{ij}^+ - \sigma_{ij}^-\right)n_i = 0$.

The weak form of Eq. (2), which is a statement of the principle of virtual work, may be formulated as

$$\int_\Omega \rho\ddot{u}_i\delta u_i\,d\Omega + \int_\Omega \sigma_{ij}\delta u_{i,j}\,d\Omega - \int_{\Gamma_1} T_i\delta u_i\,d\Gamma = 0, \tag{8}$$

where δu_i satisfies all boundary conditions on Γ_2. Using constitutive Eq. (2), and then the strain–displacement relation listed above, Eq. (8) can be explicitly expressed as in terms of displacement vector u_i. As detailed in [15], the procedure for solving an impact problem using FEM begins with constructing a mesh of elements to approximate the field functions using their values at nodes in the problem domain. However, it is very difficult to simulate the breakage of ice into a large number of fragments, as illustrated in Fig. 1, using FEM that is essentially based on continuum mechanics [18]. Fig. 1 represents a model for an ice knife. The ice knife is a solid steel wedge beneath the ship that cuts any ice that gets that far.

Cutting ice with an ice knife is an engineering problem where transition from continua to discontinua plays a major role. Transition from continua to discontinua is a result of fracture in ice which occurs through alteration, damage, yielding or failure of microstructural elements of the material. Failure, fracture and fragmentation are also observed in rock blasting operation [19].

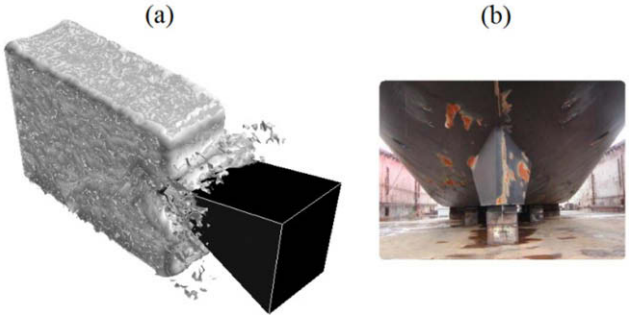

Fig. 1. (a) An ice block collides with a solid steel wedge that is a simplified model for an ice knife as shown in (b).

The EFG method has been successfully utilized by Krysl and Belytschko [20] for modeling 3D dynamically propagating cracks in elastic bodies. Their method requires only the domain boundary is explicitly represented. The domain is filled with nodes and integration points and the field function interpolant is constructed without reference to any explicit connectivity between the nodes.

Following Krysl and Belytschko [20], a shape function is constructed to approximate the vector field function, u_i, using their values at nodes in the problem domain Ω. For the sake of simplicity, a vector notation, $\boldsymbol{X}$, will be used hereafter instead of the indicial notation X_j. The approximation of u_i at a point $\boldsymbol{X}$ may be given as [18] $u_i^{(h)}(\boldsymbol{X}) = \phi_l(\boldsymbol{X})u_{li}$, where ϕ_l is the MLS shape function defined as $p_p(\boldsymbol{X})\left(A_{pq}^{-1}(\boldsymbol{X})B_{ql}(\boldsymbol{X})\right)u_{li}$ $(l = 1,\ldots,n)$ is a set of nodal values for the vector field function at n nodes $(\boldsymbol{X}_1,\ldots,\boldsymbol{X}_n)$ that are in the support domain, A_{mq} is the moment matrix given as $W_l(\boldsymbol{X})P_{pq}(\boldsymbol{X}_l)$, $p_p(\boldsymbol{X})$ $(p = 1,\ldots,m)$ is the polynomial basis, m is the number of terms of monomials, P_{pq} is the indeterminate vector product of p_p and p_q, B_{ql} is given as

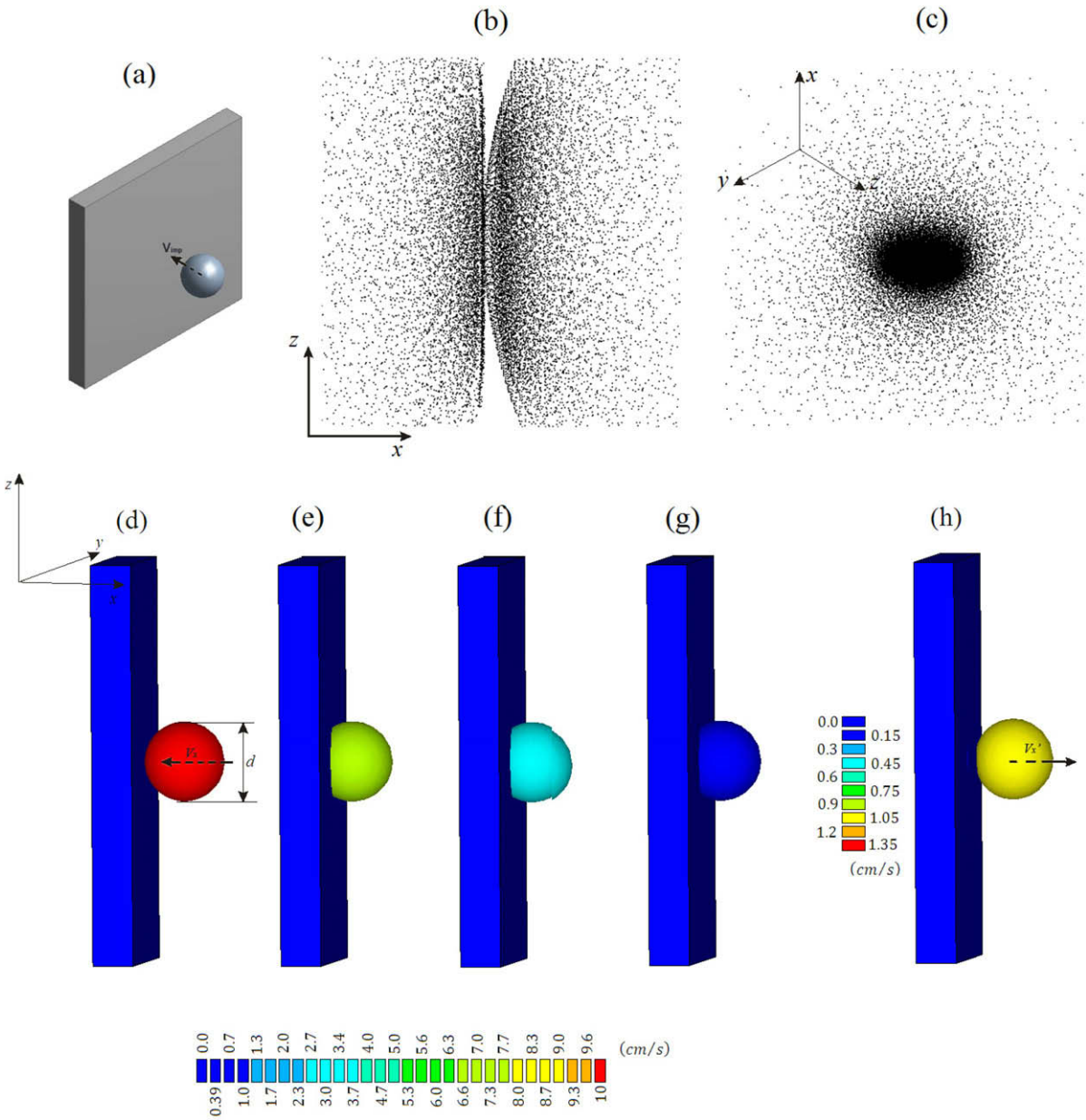

Fig. 2. (a) A model for an ice ball and an ice block. (b) A side view of the nodes scattered in the ice ball and the ice block and their boundaries. (c) A perspective view of (b). (d) The ice particle with velocity of $V_x = -10$ cm/s approaches the stationary ice block. Notice that the ice block is held stationary during the collision process. (e) and (f) Different states during the collision process. Notice that the velocity of ice ball gradually decreases. (g) The end of approach period, when the ice ball has momentarily stopped. The ice ball deformation is exaggerated for demonstration. (h) The ice ball at the end of collision process. In this case, the collision time t_c is 1.2×10^{-4} s.

$W_l(\boldsymbol{X})p_q(\boldsymbol{X})$, and $W_l(\boldsymbol{X})$ is a weight function defined as $W(\boldsymbol{X}-\boldsymbol{X}_l)$ [18]. Note that in the present study the so-called summation convention is used.

The problem of collision between a viscoelastic ice ball and a stationay ice block (which will be discussed in the following section) can be solved using the gridless approach as described above. Eq. (2) can be solved by utilizing least square interpolants to express both the trial and test functions along with the Galerkin weak form (8).

3. Collision of an ice ball with a stationary ice block

Brudges et al. [3] have designed a *real* experimental device to measure the coefficient of normal restitution of ice particles colliding with a stationary ice block. The impact velocity was in the range of 0.01–5 cm/s. They have attached an ice ball to an oscillator and let it strike a block of ice, which was held stationary. The ambient temperature was at 150–175 K. Like most solid substances, the coefficient of normal restitution of ice was found to decrease with increasing impact velocity. However, the scattering of the data has been considerably larger than the typical measurement uncertainty, which has been reported in [3].

The experimental mathematics [21,22] described in this section, may provide a compelling way to generate understanding and insight, as well as to generate and confirm or confront conjectures. In the following, the results of Brudges et al. [3] are reproduced using a mathematical model. Following Liu [18], the ice ball and the ice block are first modeled, as shown in Fig. 2(a). They are represented using sets of nodes scattered in the ball and block and their boundaries, as depicted in Fig. 2(b). Fig. 2(c) represents a perspective view of the sets of nodes generated to represent the problem domain. As can be seen, the nodal distribution is nonuniform, and a denser distribution of nodes is used in the contact area where the displacement gradient is large.

Utilizing Eq. (8), the components of the displacement at any point $\boldsymbol{X}$ within the problem domain, as shown in Fig. 2(c), is interpolated using the displacements at their nodes within the support domain of the point at $\boldsymbol{X}$. As mentioned in the preceding section, u_{li} $(i=1,2,3)$, are the components of nodal displacement vector at the node in the support domain (whose size is nodes). Here, the same shape function, ϕ, is used for all three components of the displacement vector in the support domain of the same point.

The discrete equations are formulated using the shape functions and a weak form system equation (8). The equations, which are a set of differential equations with respect to only time, are solved using the explicit method to obtain the time history of displacement, velocity, and acceleration.

The relaxation function used in the model is given by $\Phi = G_\infty + (G_0 - G_\infty)e^{-t/\tau}$. Recall that the average ice temperature in [3] was 162.5 K. Thus, the value of Young's modulus may be estimated as 15.3 GPa using Eq. (1). The value of G_0 can be found using an expression given for shear modulus, $G_0 = E/2(1+\nu) = 5.77$ GPa. Notice that the value of Poisson's ratio for ice is given in [2]. The value of G_∞ is set to zero, due to lack of knowledge. Moreover, the trial value for the relaxation time τ is selected as 10^{-5} s.

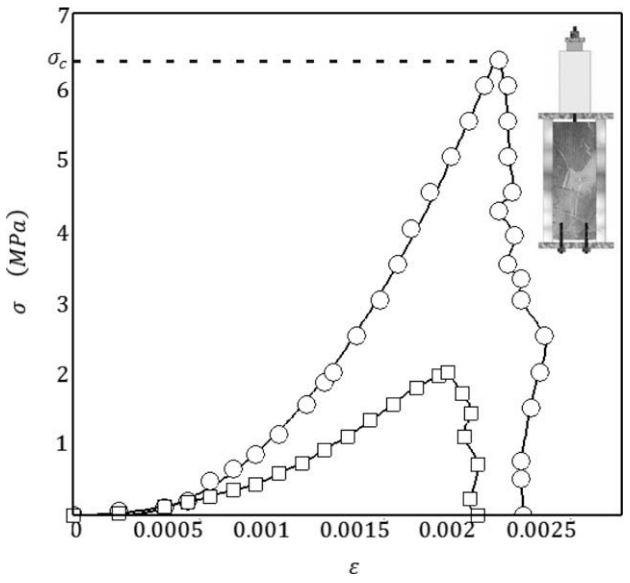

Fig. 3. Complete stress–strain curves for super-brittle ice illustrating the stiffness, (or modulus, E) the strength, σ_c, and super-brittleness. Circles and squares indicate stress–strain curves for a test specimen is loaded such that the major stress, σ_1, represented by circles is vertical and the minor, σ_2, represented by squares is horizontal. In this case, the failure strain is approximately 0.2%. The inset shows a bi-axial compression test apparatus.

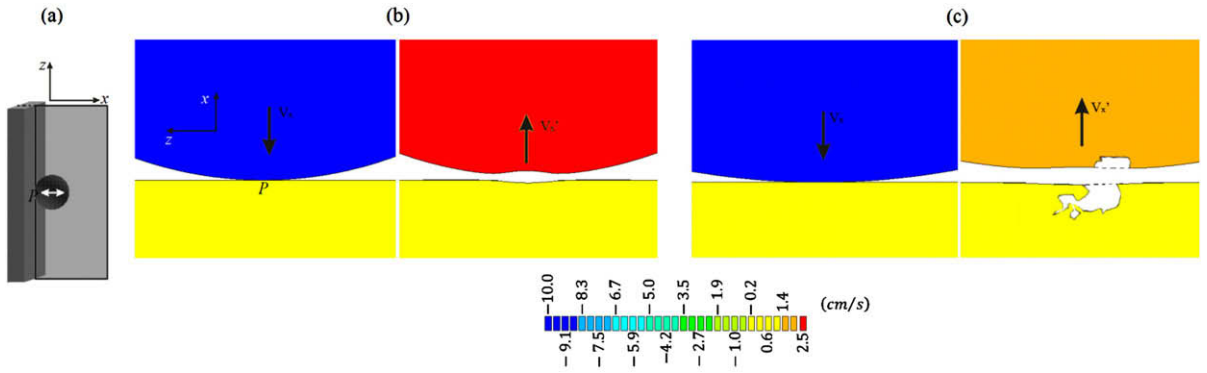

Fig. 4. (a) An elastoplastic ice ball strikes a stationary ice block. The point of initial contact is denoted as P on a xz-cutting plane. (b) From initial to terminal velocity states with no fracture. The ice ball and the ice block deformations are exaggerated for demonstration. (c) From initial to terminal velocity states with fractures. The fractures (whose sizes are exaggerated for demonstration) are shown on a xz-cutting plane. In this case, the collision time t_c is 3.2×10^{-4} s.

Fig. 2(d) illustrates an ice sphere with velocity of 10 cm/s approaches from right to a stationary ice block, which is held stationary during the collision.

Fig. 2(e)–(h) represents a gradual change in the velocity of the ice ball, from initial to terminal velocity states during the collision process. At the end of approach period, when the ice ball has momentarily stopped and is about to rebound, its kinetic energy becomes zero and its elastic deformation is maximum, as illustrated in Fig. 2(g).

As can be seen from Fig. 2, the collision is inelastic and dissipates the kinetic energy. In this case, the value for the coefficient of normal restitution may be calculated approximately using the expression $e_N = |V'_x|/|V_x| \cong 0.147$. The data of Brudges et al. [3] can be fitted with a power law

$$e_N = (0.32 \pm 0.02) V_{\text{imp}}^{-0.234 \pm 0.008} \tag{9}$$

where V_{imp} is measured in cm/s. Comparison of the model prediction with the experimental results shows that the model error is only 15%. Notice that the model prediction may be improved if a realistic value can be found for the long time shear modulus.

The lesson from the above example is that the wrong model can predict the data of Brudges et al. [3] reasonably well. In this light, it remains unclear whether the data reported in [3] can be used to validate the model of Brilliantov et al. [11], which has been developed for collision between viscoelastic particles. Notice that Brudges et al. [3] have been stated that most of the kinetic energy dissipation occurred as a result of fracturing at the contact surface area of ice particles. In the following, the experimental mathematics will be used to further confront conjectures made by Brilliantov et al. [11].

In collision processes reported in [3], the stress relaxation time cannot be expected to be in the order of the collision time, which was 10^{-4} s. The implication was plastic flow initiated cracks. If the cracks were tolerated, the ice balls have exhibited

Table 1
The physical properties of materials used in the simulations.

Property	Ice	Steel
Bulk density (g/cm^3)	0.916	7.8
Dielectric constant at 273 K	94	–
Isothermal Young's modulus at 268 K (MPa)	9.5	206
Young's modulus for snow ice (MPa)	$(23815.2 - 67.3T)$	–
Speed of longitudinal sound at 273 K (km/s)	3.8	–
Poisson's ratio	0.33	0.25
Bulk modulus 272 K (GPa)	8.8	–
Shear modulus 272 K (GPa)	3.9	–
Adiabatic bulk compressibility at 273 K (10^{-11} Pa)	12	–
Thermal conductivity at 263 K (W/mK)	2.23	–
Instantaneous (glassy) shear modulus at 162.5 K (GPa)	5.77	–
Long time shear modulus	0	–
Relaxation time (s)	10^{-5}	–
First Cowper–Symonds strain rate parameter (s^{-1})	25	–
Second Cowper–Symonds strain rate parameter	3	–
Hardening parameter	0.5	–
Yield stress (MPa)	6.3	–
Tangential modulus (MPa)	100	–
Failure strain	0.25%	–

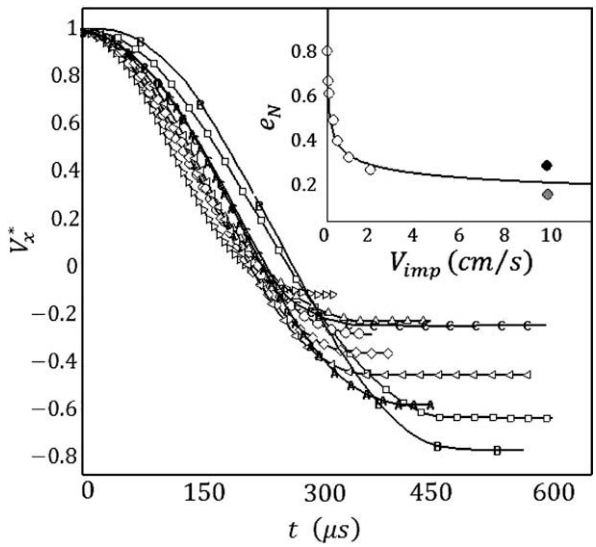

Fig. 5. Variations of the normalized velocity, $V_x^* = V_x/V_{\text{imp}}$, of the center of mass of the ice ball as a function of time at several different impact velocities. Left triangles and "C" represent collisions at impact velocities of 10 cm/s, as illustrated in Fig. 4(c) and (b), respectively. Triangles, circles, diamonds, left triangles, "A", squares, and "B" represent collisions at impact velocities of, 2, 1, 0.5, 0.3, 0.1, 0.05, 0.01 cm/s, respectively. The inset shows the coefficient of normal restitution versus impact velocity. Black and gray circles represent cases whose results are shown in Fig. 4(b) and (c), respectively. The solid line and dashed lines are graphs of $e_N = 0.311V_{\text{imp}}^{-0.238}$, and $e_N = 0.32V_{\text{imp}}^{-0.234}$ according to Eqs. (11) and (9), respectively.

macroscopically ductile behavior. If not, then the ice balls have exhibited macroscopically brittle behavior. Fig. 3 represents a typical stress–strain curve for ice consists of the hardening branch (before the peak stress, σ_c, is reached) and strain-softening part, which represents decreasing stress with increasing strain.

Here, the main goal is to model multiple-crack situations, progressive fracture and failure, including fragmentation and the creation of a large number of ice fragments of general shape and size, as shown in Fig. 1(a). To this end, approximations are used for stress–strain curves of ice, as illustrated in Fig. 3. Fig. 3 also illustrates a bi-axial compression test apparatus for ice. Notice that biaxial means for providing support along two directional axes of the ice sample.

A rate-sensitive plasticity material model for ice with failure is utilized to predict experimentally measured coefficient of normal restitution reported in [3], and thus demonstrate that a suitable model for ice has been developed. The model as shown in Fig. 4(a) includes an ice ball, and a stationary ice block. Rate effects on the yield stress can be modeled by a Cowper–Symonds strain-rate model [23], given as

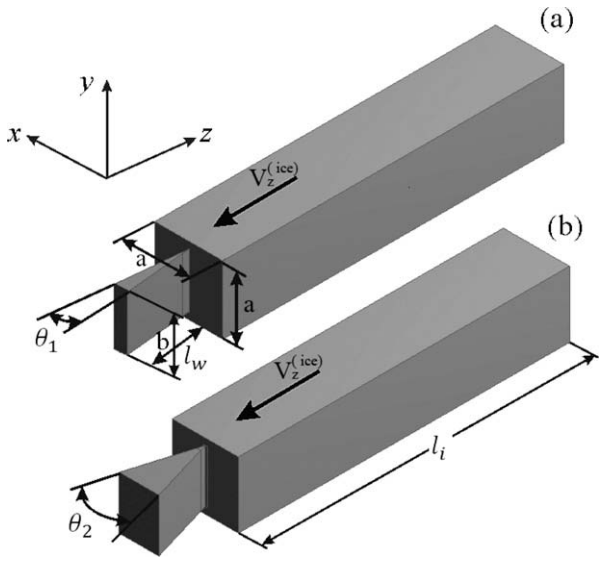

Fig. 6. Models for the ice knife (a) small angle, and (b) large angle. Here, V_z represents the velocity of the ice block relative to the solid wedge. Here, $\theta_1 = 12^\circ$, $\theta_2 = 30^\circ$, $a = 0.15$ m, $l_w = 0.35$ m, $b = 0.12$ m, $l_i = 0.95$ m.

$$\sigma_Y = \left(1 + \left(\frac{\dot{\varepsilon}}{c}\right)^{\frac{1}{q}}\right)(\sigma_0 + \beta E_p \varepsilon_p). \tag{10}$$

Of primary interest are the material properties utilized in modeling the ice ball and the ice block as shown in Fig. 4(a). Table 1 summarizes the material inputs used in the model. Properties such as bulk density and Poisson's ratio are taken from [2]. Values for yield stress and failure strain are determined from the experimental results as show in Fig. 3. In addition, values for the first and second Cowper–Symonds strain rate parameters are parametrically determined by comparing the numerical results with the experimental data reported in [3].

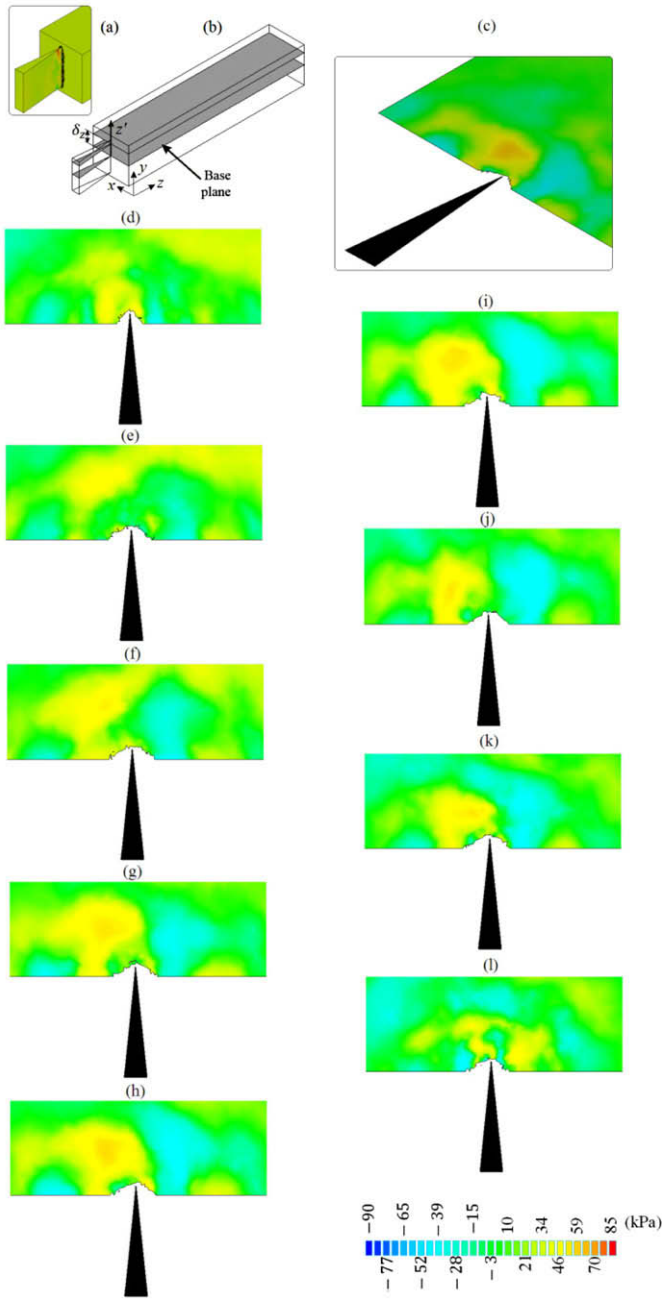

Fig. 7. (a) A perspective view of a stationary, small angle wedge made from steel penetrates into a moving ice block whose velocity is $V_z = -2$ m/s. Sample results are taken after $t = 10^{-2}$ s. (b) The position of a sampling xz' plane located at $z' = \delta_z$ with respect to a base xz' plane located at $z' = 0$. (c) A perspective view of the contour plot of the xz' off-diagonal component of the shear stress tensor on the base cutting plane (namely, $\delta_z = 0$). (d)–(i) A top view of the contour plots of the xz' off-diagonal component of the shear stress tensor on the cutting planes located at $\delta_z = 12$, 9, 6, 3, 0, −1.5, −4.5, −7.5, and −10.5 cm, respectively.

As stated earlier, the EFG method allows simulating crack evolution by adding nodes around the crack tip to capture the stress concentration with desired accuracy. This nodal refinement can be moved with a propagation crack through a background arrangement of nodes associated with the global geometry.

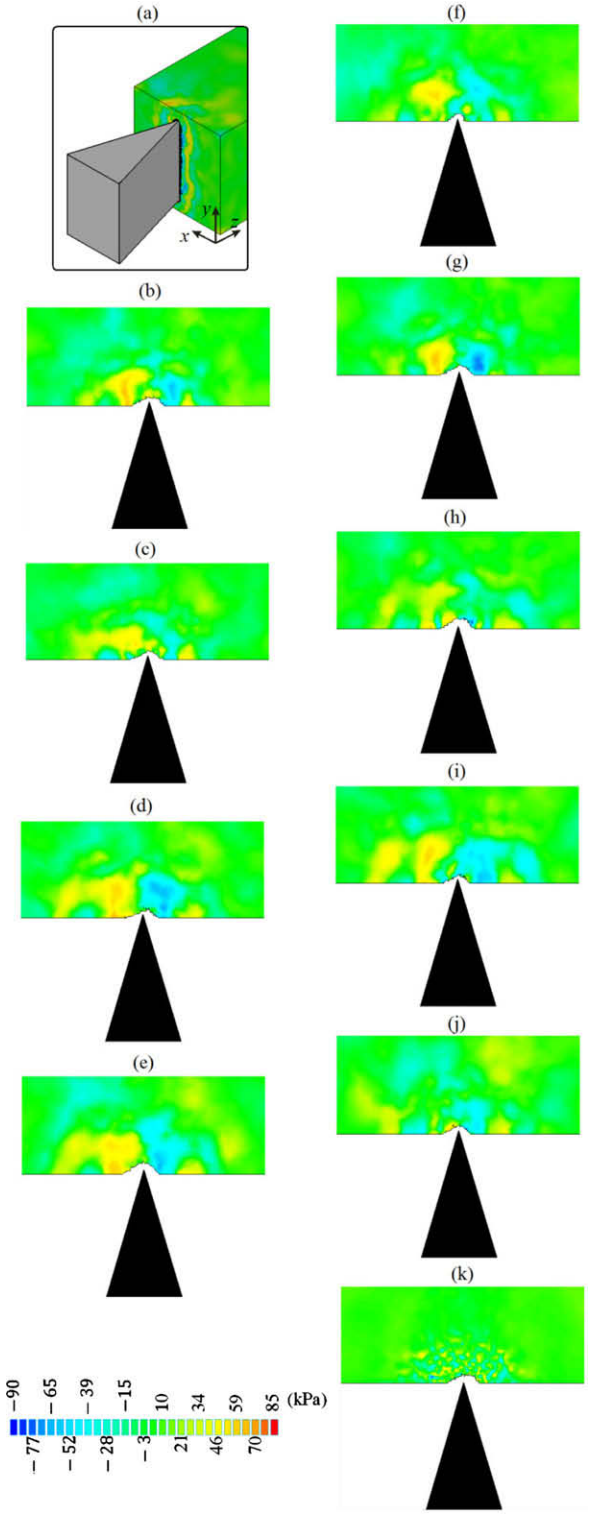

Fig. 8. (a) A perspective view of a stationary, large angle wedge made from steel penetrates into a moving ice block whose velocity is $V_z = -2$ m/s. Sample results are taken after $t = 10^{-2}$ s. (b)–(k) A top view of the contour plots of the xz' off-diagonal component of the shear stress tensor on the cutting planes located at $\delta_z = 12,\ 9,\ 6,\ 3,\ 0,\ -1.5,\ -4.5,\ -7.5$, and -10.5 cm, respectively.

The model predictions as shown in Figs. 4 and 5 agree with the experimental data [3]. For example, Fig. 4(b) and (c) represents two different values for the coefficient of restitution at the same impact velocity. Notice that values for yield stress and failure strain used in the second simulation whose results are shown in Fig. 4(c) are 2.2 MPa, and 0.19%, respectively. The results of Fig. 4 imply that crack formation can reduce the coefficient of restitution by 40%. Notice that the simplified model used in this study may be used to interpret the dispersion of data in [3].

Schulson has stated that ice is quite complicated and whose inelastic behavior is markedly anisotropic [2]. The results of Fig. 4 highlight that the ice balls used by Bridges et al. [3] were not exactly the same, and thus different values for the coefficient of restitution were measured at nearly the same impact velocity.

The results presented in Fig. 5 can be fitted with a power law

$$e_N = 0.311 V_{\text{imp}}^{-0.238}. \tag{11}$$

As shown in the inset of Fig. 5, the best fitted curve (11) becomes nearly identical with the power law (9) reported in [3].

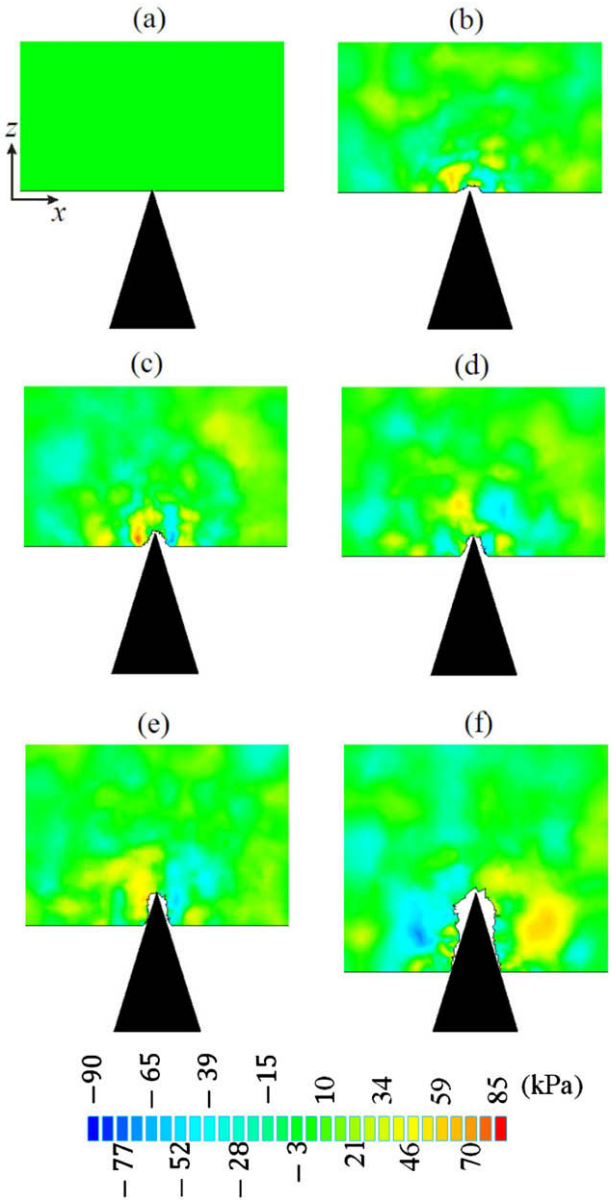

Fig. 9. Evolution during dynamic crack propagation in a moving ice block with the velocity of $V_z = -2$ m/s. Shown are the contour plots of the xz off-diagonal component of the shear stress tensor on the cutting planes located at $\delta_z = 0$. (a)–(f) The samples are taken after $t = 0, 10^{-2}, 2.5 \times 10^{-2}, 3.5 \times 10^{-2}, 5.5 \times 10^{-2}$ and 8.5×10^{-2} s.

In brief, it may be concluded that the simplified viscoelastic model of Brilliantov et al. [11] may not be suitable for representing such a complex material such as ice.

4. Ice–structure collisions

A reliable model for ice has been developed in the preceding section and is now applied to predicting compressive failure in recognition of the practical importance of the phenomenon in ice–structure interactions.

An icebreaker has what is called an ice knife. This is not the type of knife one might immediately imagine. It is basically a projection of solid steel (or wedge), as schematically shown in Fig. 6, located below the bow that helps prevent the ship from riding too far up onto heavy ice and effectively beaching itself or having ice travel under the hull to the propellers. A real ice knife is illustrated in Fig. 1(b).

The aim is to determine an optimal wedge angle for breaking ice like a hot knife through butter. To this end, basic steps are made including domain representation, displacement interpolation, formation of system equations, and finally solving the global gridless equations. Enhancement functions are added to produce stress fields singularity at the crack tip and stress discontinuity at interfaces of the moving ice block and the wedge. Notice that the wedge, as illustrated in Fig. 6, is assumed to behave as an elastic solid. Again, Table 1 summarizes the basic material inputs used in the model as described in the preceding section.

For this problem the ice domain involves multiple discontinuities, such as multiple cracks, as illustrated in Figs. 8–13. Thus, the support (influence) domain contains numerous irregular boundary fragments. In this case, a hierarchical network of relay points is constructed to transmit nodal influence from the source node is to the blocked areas.

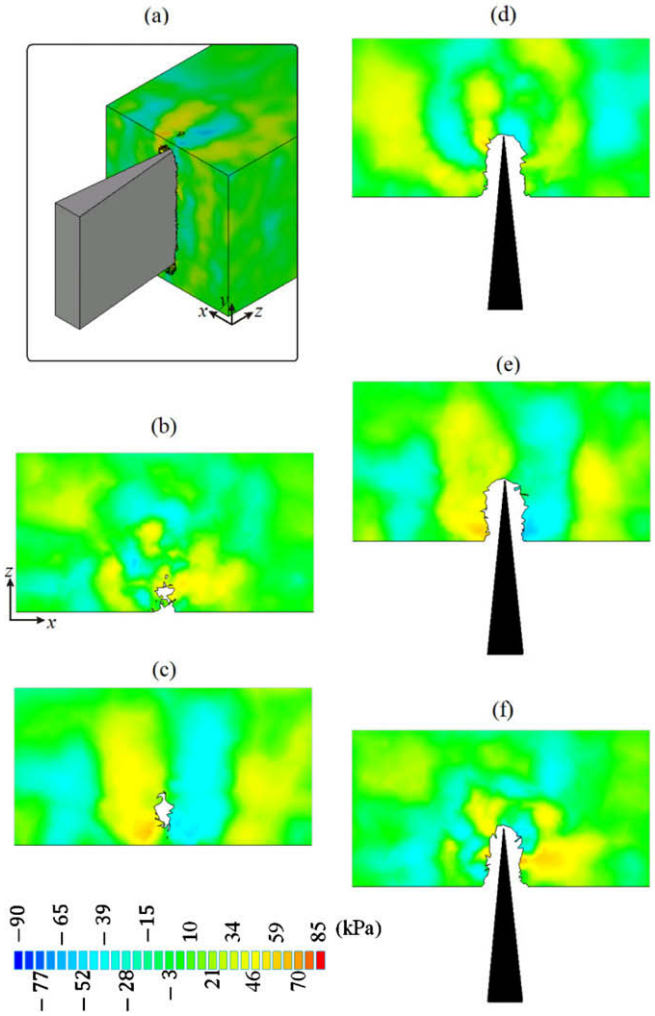

Fig. 10. (a) A perspective view of a stationary, small angle wedge made from steel penetrates into a moving ice block whose velocity is $V_z = -2$ m/s. Sample results are taken after $t = 6 \times 10^{-2}$ s. (b)–(f) A top view of the contour plots of the xz' off-diagonal component of the shear stress tensor on the cutting planes located at $\delta_z = 15,\ -15,\ 6,\ 0,$ and -6, respectively. Notice that the upper and lower faces of the ice block are also damaged.

Fig. 7 represents that the movement of small-angle wedge tip with respect to ice block results in the formation of radial cracks that propagate towards the end of ice block. Apparently, there is no significant difference in crack propagation processes when a large-angle wedge instead of small-angle wedge penetrates into the ice block, as evidenced from Fig. 8.

Fig. 9 represents evolution during dynamic crack propagation in a moving ice block. As can be seen, as the stress wave reflects from the free surface, it is followed by cracks that propagate toward the cavity.

Fig. 10 represents a minor damage on the free surface of the ice block. In addition, more cracks that propagate toward the cavity can be observed in Fig. 10(d)-(f).

Fig. 11 represents a moderate damage on the free surface of the ice block when the large-angle wedge is deeply penetrated into the ice block at $t = 0.1$ s. Notice that the height of the wedge is shorter than the height of the ice block, as illustrated in Fig. 6.

Fig. 12 represents a severe damage on the free surface of the ice block, provided the wedge can freely move in the direction normal to the relative velocity of the ice block and the wedge. The damage is even more pronounced if the small-angle wedge is used instead the large-angle wedge, as shown in Fig. 12.

Fig. 13 suggests that in order to break ice like a hot knife through butter the wedge has to free to rotate around its axis which is perpendicular to the direction of the relative velocity of the wedge and the ice block. In this case, the fragmentation process accelerates resulting in a network of interconnected cracks together with a large number of separate ice fragments in transient motion, as shown in Fig. 13(b). Finally, the block of ice is cut in pieces, as shown in Fig. 13, which would be the task of an effective ice knife in an icebreaker.

Notice that the results presented in this section can be used to develop a novel damage detection technique, tailored at the identification of ice structure damage beneath the icebreaker. The damage detection exploits the wave propagation phenomena by identifying discrepancies, due to damage presence, in the dynamic behavior of the ice block. The uncorrelations are generated by waves reflected back to the sensor locations by the flaw surfaces. The arrival time of the reflected wave may be estimated using the wavelet transform [24]. Then, the detection algorithm is able, through a ray-tracing algorithm, to estimate the location of damage, as shown in Fig. 12. This method will be discussed in details in a future paper.

The model as discussed in this section can also be utilized in modeling offshore structures in the regions subjected to annual winter sea moving ice which can damage the structures.

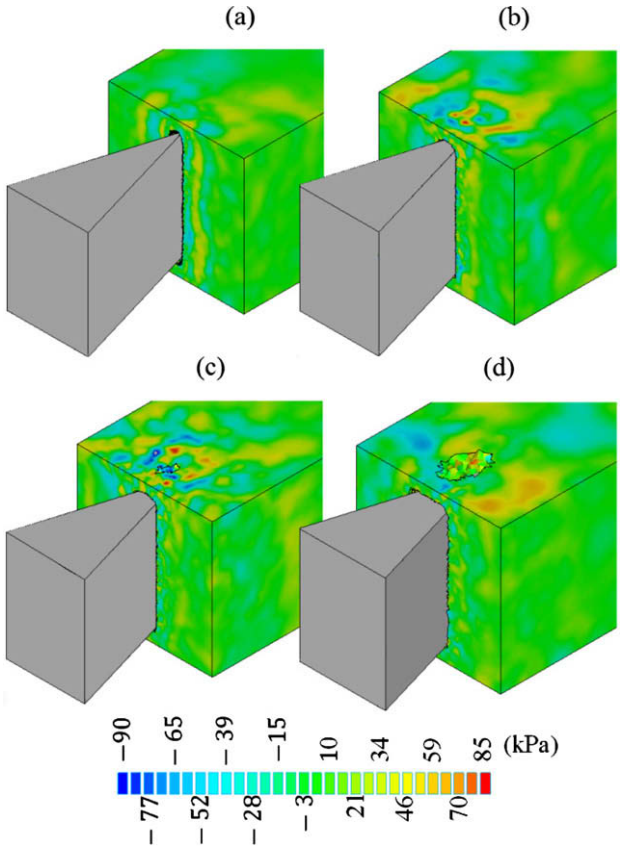

Fig. 11. Evolution during dynamic crack propagation in a moving ice block with the velocity of $V_z = -2$ m/s. Shown are the contour plots of the *xz* off-diagonal component of the shear stress tensor on the perspective views of the ice block at $t = 10^{-2}$, 6×10^{-2}, 8×10^{-2} and 9×10^{-2} s.

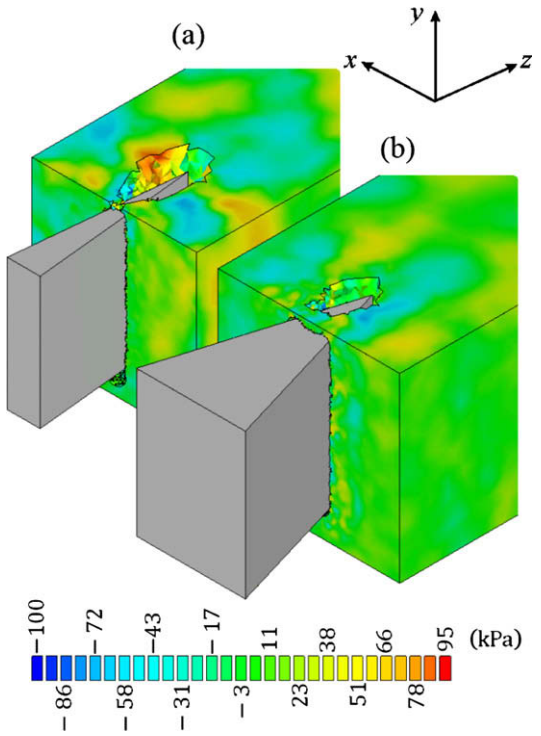

Fig. 12. The perspective views of (a) the small-angle wedge and (b) the large-angle wedge made from steel penetrate into a moving ice block whose velocity is $V_z = -2$ m/s. Sample results are taken after $t = 8 \times 10^{-2}$ s. Here, the wedges both can move freely in the y-direction, but their movements in the x and z-direction are restricted. Shown are the contour plots of the off-diagonal component of the shear stress tensor on the perspective views of the ice block.

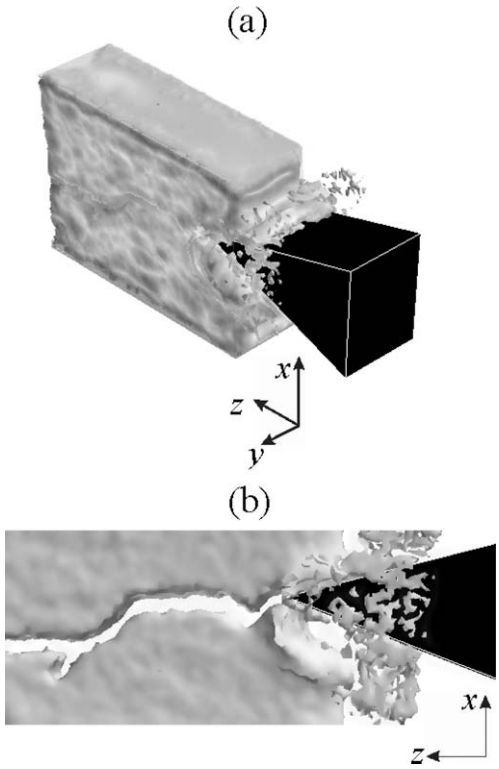

Fig. 13. (a) A perspective view of the large-angle wedge breaks a moving ice block whose velocity is $V_z = -2$ m/s. Sample results are taken after $t = 7.5 \times 10^{-2}$. The center of mass of the wedge is fixed, but it can rotate freely around the y-axis. (b) A side view of fractured ice, including fragmentation and the creation of a large number of ice fragments of general shape and size.

5. Conclusions

The element-free Galerkin (EFG) method utilizes the gridless method for solving the governing partial differential equations. The EFG method has been utilized to predict collisional behavior of ice particles. Ice is quite complicated and whose inelastic behavior is markedly anisotropic. An impressive agreement has been obtained between the model predictions and the experimental data [3]. The developed model may be further used:

- To assist in selecting an optimal cone to be fitted to the legs of offshore structures to alleviate the dynamic forces produced by the moving ice.
- To investigate hail ice impacts which are a realistic threat to exposed composite structures such as aircraft fuselage and wing skins, leading-edge and control surfaces, engine nacelles, and fan blades.
- To predict the threshold of critical damage to the orbiter's wing leading edge from ice debris impacts.

References

[1] Eisenberg D, Kauzmann W. The structure and properties of water. Oxford: Clarendon Press; 1969.
[2] Schulson EM. The structure and mechanical behavior of ice. J JOM 1999;51:21–7.
[3] Bridges FG, Hatzes A, Liu DNC. Structure, stability and evolution of Saturn's rings. Nature 1984;309:333–5.
[4] Weeks WF, Ackley SF. The growth structure and properties of sea ice. In: The geophysics of sea ice. Dordrecht: Martinus Nijhoff; 1986.
[5] Perutz MF. A description of the iceberg aircraft carrier and the bearing of the mechanical properties of frozen wood pulp upon some problems of glacier flow. J Glaciol 1948;1:95–102.
[6] Sanderson TJO. Ice Mechanics risks to offshore structures. London: Graham & Trotman; 1988.
[7] Godbout S, Chenard L, Marquis A. Instantaneous Young's modulus of ice from liquid manure. Can Agric Eng 2000;42:95–100.
[8] Lindgren S. Thermal ice pressure. In: Proceedings of IAHR symposium, ice and its action on hydraulic structures; 1970. p. 6.7.1–40.
[9] Hatzes AP, Bridges FG, Lin DNC. Collisional properties of ice spheres at low impact velocities. Mon Not R Astr Soc 1988;231:1091–115.
[10] Goldsmith W. Impact: the theory and physical behaviour of colliding solids. New York: Dover; 2001.
[11] Brilliantov NV, Spahn F, Hertzsch JM, Poschel T. Model for collisions in granular gases. Phys Rev E 1996;53:5382–92.
[12] Liebowitz H, Moyer Jr ET. Finite element methods in fracture mechanics. Comput Struct 1989;31:1–9.
[13] Aliabadi MH. Boundary element formulations in fracture mechanics. Appl Mech Rev 1997;50:83–96.
[14] Belytschko T, Lu YY, Gu L. Crack propagation by element-free Galerkin methods. Eng Fract Mech 1995;51:295–315.
[15] Zamankhan P, Bordbar M-H. Complex flow dynamics in dense granular flows. Part I: experimentation. J Appl Mech (T-ASME) 2006;73:648–57.
[16] Zamankhan P, Huang J. Complex flow dynamics in dense granular flows. Part II: simulations. J Appl Mech (T-ASME) 2007;74:691–702.
[17] Mase GE. Continuum mechanics. New York: McGraw-Hill; 1970.
[18] Liu GR. Mesh free methods. Boca Raton (FL): CRC Press; 2003.
[19] Hudson JA, Harrison JP. Engineering rock mechanics. Amsterdam: Pergamon Press; 2000.
[20] Krysl P, Belytschko T. The element free Galerkin method for dynamic propagation of arbitrary 3-D cracks. Int J Numer Meth Eng 1999;44:767–800.
[21] Borwein J, Bailey D. Mathematics by experiment: plausible reasoning in the 21st century. A.K. Peters, Natick, Massachusetts, USA; 2004.
[22] Borwein J, Bailey D, Girgensohn R. Experimentation in mathematics: computational paths to discovery, A.K. Peters, Natick, Massachusetts, USA; 2004.
[23] Paik JK, Thayamballi AK. Ship-shaped offshore installations. Cambridge: Cambridge University Press; 2007.
[24] Zamankhan P, Mazouchi A, Sarkoma P. Some qualitative feature of couette flow of monodisperse granular materials. Appl Phys Lett 1997;71:3790–2.